1   **In situ architecture and cellular interactions of polyQ inclusions**

2   Felix J. Bäuerlein[1], Itika Saha[2, *], Archana Mishra[3, *], Maria Kalemanov[1, 4], Antonio Martínez-Sánchez[1],

3   Rüdiger Klein[3, 5], Irina Dudanova[3], Mark S. Hipp[2, 5], F. Ulrich Hartl[2, 5, ¶], Wolfgang Baumeister[1, ¶, #] and

4   Rubén Fernández-Busnadiego[1]

5   [1] Department of Molecular Structural Biology, Max Planck Institute of Biochemistry, 82152 Martinsried,

6   Germany.

7   [2] Department of Cellular Biochemistry, Max Planck Institute of Biochemistry, 82152 Martinsried,

8   Germany.

9   [3] Department of Molecules - Signaling – Development, Max Planck Institute of Neurobiology, 82152

10   Martinsried, Germany.

11   [4] Graduate School of Quantitative Biosciences Munich, 81337 Munich, Germany.

12   [5] Munich Cluster for Systems Neurology (SyNergy), D-80336 Munich, Germany.

13

14   * These authors contributed equally

15   ¶ Correspondence to: uhartl@biochem.mpg.de, baumeist@biochem.mpg.de

16   # Lead contact

17

18   **Summary**

19

20   Expression of many disease-related aggregation-prone proteins results in cytotoxicity and the formation

21   of large intracellular inclusion bodies (IBs). However, the role of IBs in pathology is not well understood,

22   and the in situ structure of protein aggregates inside cells has not yet been determined. Here we employ

23   advanced cryo-electron tomography (cryo-ET) methods to analyze the structure of IBs formed by

24   polyglutamine (polyQ)-expanded huntingtin exon 1 within their intact cellular context and to an

25   unprecedented level of detail. We find that in primary mouse neurons and immortalized human cells,

26   polyQ IBs consist of amyloid-like fibrils that interact with cellular endomembranes, particularly those of

27   the endoplasmic reticulum (ER). The interactions with these fibrils lead to membrane deformation, the

28   local impairment of ER organization and profound alterations in ER membrane dynamics at the IB

29   periphery. These results suggest that aberrant interactions between IB fibrils and endomembranes

30   contribute to the deleterious cellular effects of protein aggregation.

Introduction

Protein aggregation is a hallmark of many neurodegenerative disorders including Huntington's disease (HD), amyotrophic lateral sclerosis and Parkinson's disease (Hipp et al., 2014; Ross and Poirier, 2004). Soluble oligomeric aggregates have been linked to toxicity in many of these proteinopathies, whereas the large insoluble IBs found in the brains of patients and in animal and cellular models are often regarded as oligomer-sequestering protective entities (Arrasate and Finkbeiner, 2012; Bucciantini et al., 2002; Haass and Selkoe, 2007). However, the exact contribution of IBs to pathology remains poorly characterized, and detailed structural information on IB organization in unperturbed cellular environments is missing. The traditional methods of sample preparation including chemical fixation, dehydration and heavy metal staining are not compatible with high-resolution structural studies.

Recent technical advances make cryo-ET ideally suited to address the challenge of studying in situ IB structures and their interactions with their cellular environment. Cryo-focused ion beam milling (cryo-FIB) opens windows into the interior of frozen-hydrated vitrified cells by producing thin lamellas that can be studied in 3D by cryo-ET (Mahamid et al., 2016; Rigort et al., 2012a). Furthermore, cryo-ET imaging capabilities have been dramatically expanded by the introduction of direct electron detectors (Qiang et al., 2013) and the Volta phase plate, which enables imaging close to focus with maximum contrast (Asano et al., 2015; Danev et al., 2014; Mahamid et al., 2016). Thus, cryo-ET allows the 3D visualization of pristinely preserved cells at molecular resolution.

Here we capitalize on these developments to dissect IB architecture within unstained, frozen-hydrated, vitrified mammalian cells, using polyQ-expanded huntingtin (Htt) exon 1 as a model aggregating protein. The expansion of a polyQ stretch in the N-terminal region of Htt renders the mutant protein highly aggregation-prone and leads to HD in humans. PolyQ-expanded Htt oligomers have been implicated in the misregulation of, among others, transcription, vesicular traffic, autophagy and the function of the

55 endoplasmic reticulum (ER) and mitochondria (Arrasate and Finkbeiner, 2012; Finkbeiner, 2011;

56 Macdonald, 1993; Scherzinger et al., 1997), but it is not known whether IBs play any roles in these

57 phenomena. Furthermore, several other neurodegenerative disorders including spinal and bulbar

58 muscular atrophy and spinocerebellar ataxias are also caused by polyQ expansions in otherwise non-

59 related proteins (Orr and Zoghbi, 2007). Our results show that polyQ-expanded Htt exon 1 IBs are formed

60 by fibrils that impinge on cellular membranes, especially those of the ER. These interactions result in

61 membrane deformation and possibly rupture, as well as impaired ER organization and dynamics around IBs.

62 **Results**

63
64 <u>Three-dimensional architecture of Htt97Q IBs</u>

65 IBs in HD patient neurons are formed by N-terminal fragments of Htt harboring the polyQ-expanded

66 exon 1, expression of which suffices to recapitulate HD-like symptoms in mice (Davies et al., 1997;

67 DiFiglia et al., 1997; Mangiarini et al., 1996; Yamamoto et al., 2000). We transfected mouse primary

68 neurons with GFP-tagged Htt exon 1 containing 97 Q (Htt97Q-GFP). Non-apoptotic cells containing IBs

69 were identified by live imaging and subsequently vitrified by plunge freezing upon a short incubation in

70 medium containing 10% glycerol to ensure full vitrification. Correlative microscopy allowed us to target

71 IBs for cryo-FIB milling to yield 150-250 nm-thick cellular lamellas that were imaged in 3D by Volta phase

72 plate cryo-ET (Fig. S 1). Htt97Q-GFP IBs were roughly spherical, ~3 µm in diameter and mostly cytosolic,

73 although nuclear IBs were also found. Both cytosolic and nuclear IBs consisted of a network of amyloid-

74 like fibrils with a diameter of 7-8 nm and length of 125 ± 81 nm (mean ± SD) (Fig. 1A, B, E, Fig. 2A, B). The

75 fibrils were radially arranged in most, but not all IBs (Fig. 1A, B, Fig. 2, Fig. 3A-C). Thus, despite the

76 similarity in fibril length, the cellular organization of Htt97Q-GFP fibrils was very different from the

77 bundles of parallel fibrils formed by Sup35 yeast prions (Kawai-Noma et al., 2010; Saibil et al., 2012). The

78 analysis of fibril curvature provided insights into their flexibility. We calculated an average fibril

79 persistence length of 2.6 ± 0.1 µm (mean ± SD) and a Young's modulus of 52 ± 2 MPa (mean ± SD) (Fig. S

80   3), in the range of other amyloid fibrils or actin (Mahamid et al., 2016; Wegmann et al., 2010). Despite

81   the dense appearance of the network, the fibrils occupied less than 3% of the IB volume (Fig. 1F).

82   In situ fibrils were morphologically similar to those formed in vitro but did not associate laterally to form

83   wider ribbons (Scherzinger et al., 1997) (Fig. 1A, inset). Interestingly, Htt97Q-GFP fibrils were decorated

84   by regularly spaced globular densities of ~6 nm in diameter consistent in size with GFP dimers. To

85   further investigate the nature of these densities, cells were co-transfected with untagged 97Q Htt exon

86   1 (Htt97Q) and mCherry-ubiquitin. The latter can be conjugated to target proteins in a manner similar to

87   wild-type ubiquitin (Qian et al., 2002) and its recruitment to IBs (Hipp et al., 2012) served as a surrogate

88   fluorescent marker for Htt97Q IBs. Given the relatively low transfection rates obtained in neurons, these

89   and further experiments were carried out in HeLa cells to increase the number of cells amenable to

90   cryo-ET analysis. Htt97Q and Htt97Q-GFP IBs in HeLa cells were almost identical to those in neurons in

91   terms of overall architecture and fibril morphology (Fig. 1E-H, Fig. 3A-C). Although Htt97Q-GFP and

92   untagged Htt97Q fibrils were similar in diameter and length (Fig. 1E), untagged Htt97Q fibrils were not

93   decorated by additional densities (Fig. 1H). This demonstrates that the fibrils consisted of Htt97Q, and

94   suggests a molecular organization in which the polyQ regions form the fibril core whereas the more

95   flexible C-terminal sequence protrudes outwards (Bugg et al., 2012; Isas et al., 2015; Lin et al., 2017).

96   The presence of GFP resulted in a 50% reduction in fibril density within the IB (Fig. 1F) and a 25%

97   increase in fibril stiffness (Fig. S 3).

98   Htt97Q and Htt97Q-GFP fibrils were always observed as part of IBs, suggesting that IBs are the main

99   sites of fibril growth in the cell (Ossato et al., 2010). Although only a small fraction of IB volume was

100   occupied by fibrils (Fig. 1F), the core of the aggregates was mostly devoid of large macromolecules such

101   as ribosomes, which were abundant at the IB periphery (Fig. 1A, B).

102

103 <u>Htt97Q fibrils impinge on cellular endomembranes</u>

104 For all cytosolic IBs analyzed (N = 5, neurons, Htt97Q-GFP; N = 10, HeLa, Htt97Q-GFP; N = 8, HeLa,

105 Htt97Q), fibrils in extended areas of the IB periphery visibly contacted the membranes of various

106 organelles. These included mitochondria, lysosomes and most prominently the ER (Fig. 1A, B, Fig. 3, Fig.

107 S 4B, D, movie 1), while no direct IB association with autophagic structures was observed. The electron

108 densities of membranes and fibrils often appeared continuous at points of contact (Fig. 1D, Fig. 3D, Fig. S

109 4D), indicating that the fibril-membrane distance was shorter than the pixel size (1.7 or 2.8 nm).

110 Ribosome-free ER tubes often protruded into the IB, apparently interacting extensively with the fibrillar

111 network (Fig. 1C, D, Fig. 3B, C, G). Both the ends and sides of fibrils directly touched the membranes, and

112 these regions displayed extremely high membrane curvature (Fig. 1C, D, Fig. 3D-F). A systematic analysis

113 showed that ER membrane curvature was higher at the IB interface than in more distal areas, as well as

114 in cells expressing diffuse Htt97Q-GFP without visible IBs or non-pathogenic Htt25Q-GFP (Fig. S 2D, Fig. S

115 4). Interestingly, a heterogeneous population of vesicles was embedded in most cytosolic IBs (100%,

116 neurons, Htt97Q-GFP; 94%, HeLa, Htt97Q-GFP; 82%, HeLa, Htt97Q) at sites of interaction with

117 organelles (Fig. 1A, B, D, Fig. 3A-F). Many of these vesicles were highly irregular in shape and were often

118 in contact with fibrils at regions of high membrane curvature, suggesting that they resulted from the

119 disruption of organellar membranes upon interaction with the fibrils (Fig. 1D, Fig. 3D-F). Ribosomes

120 were bound to the membranes of some of these vesicles, suggesting that they originated from ruptured

121 ER membranes (Fig. 3E, F). Comparable IB architecture and membrane interactions were found in cells

122 expressing Htt64Q-GFP (Fig. 2C, D), arguing against a strong influence of the exact length of the

123 expanded polyQ tract on fibril arrangement and cellular interactions. Interestingly, similar membrane

124 deformations at contact regions with amyloid fibrils leading to membrane disruption were previously

125 observed in vitro with liposomes (Milanesi et al., 2012). Nuclear IBs were similar in overall architecture

126 to cytosolic IBs but did not contain vesicles nor did they contact the inner nuclear membrane (Fig. 2A, B),

127   indicating differential mechanisms of cellular interaction (Benn et al., 2005; Gu et al., 2015; Liu et al.,

128   2015). In summary, the fibrils forming cytosolic polyQ IBs have the potential to deform and perhaps

129   disrupt cellular membranes in their proximity, particularly those of the ER, both in mouse neurons and

130   human cells.

131

132   <u>Htt97Q IBs alter ER organization and dynamics</u>

133   Light microscopy experiments in HeLa cells confirmed the association of Htt97Q-GFP IBs with the ER (Fig.

134   4A). Interestingly, some IBs contained puncta positive for ER markers but disconnected from the ER

135   network (Fig. 4B), in line with the assumption that some of the vesicles found within IBs by cryo-ET

136   originated from ruptured ER membranes. Occasionally, puncta positive for mitochondrial markers were

137   also observed inside Htt97Q-GFP IBs (Fig. S 4A), but this was not the case for other organelles such as

138   the Golgi apparatus (Fig. S 4C). Thus, our light and electron microscopy data indicate that the polyQ Htt

139   exon 1 fibrils of IBs interact most extensively with ER membranes.

140   We further investigated the consequences of this membrane interaction by immunostaining for a

141   variety of ER-resident proteins. Interestingly, some ER chaperones (e.g. calnexin) and components of the

142   ER-associated degradation (ERAD) machinery (e.g. Erlin-2, Sel1L) were enriched in the ER domain

143   surrounding the IBs, whereas other ER proteins (e.g. BiP, calreticulin, PDI or p97) did not show this

144   pattern (Fig. S 4E and data not shown). In contrast, the translocase component Sec61 was largely

145   excluded from the IB vicinity, consistent with the observation by cryo-ET that ER membranes in contact

146   with the IB were essentially devoid of ribosomes (Fig. 1C, Fig. 3C, G). Thus, some but not all of the

147   components of the so-called ER quality control compartment (Leitman et al., 2013a) accumulated

148   around Htt97Q-GFP IBs. Strikingly, live cell imaging revealed a complete "freezing" of ER dynamics in the

149   vicinity of Htt97Q-GFP IBs (Fig. 4C-F, Fig. S 4F-H, movie 2). This effect was not merely steric, as the ER

150   was highly dynamic around other large cellular structures or the nucleus (Fig. 4C, D). Altogether, these

151   data suggest that the interaction of Htt97Q-GFP fibrils with ER membranes alters cell physiology by

152   locally impairing ER organization and dynamics.

153   **Discussion**

154   While polyQ-expanded Htt exon 1 forms fibrils in vitro (Scherzinger et al., 1997), it has remained

155   controversial whether Htt in cellular IBs is present in granular or fibrillar form (Finkbeiner, 2011; Qin et

156   al., 2004; Waelter et al., 2001). Importantly, fibril formation is thought to be required for

157   neurodegeneration in mice (Gu et al., 2009). Our cryo-ET data conclusively show that in vitrified frozen

158   hydrated murine neurons and human cells, IBs of polyQ-expanded Htt exon 1 consist of fibrils. The high

159   resolution of our images allowed us to resolve additional densities decorating the fibrils formed by a

160   GFP-labeled Htt97Q construct, and to quantify the changes in fibril density and rigidity induced by the

161   GFP tag. Htt97Q fibrils were substantially thinner than those found in heavy-metal stained preparations

162   (Qin et al., 2004), and sufficiently stiff to deform membranes (Roux, 2013). The structure of in situ fibrils

163   is consistent with that proposed by recent NMR studies, in which the polyQ stretch forms the amyloid

164   core and the flanking regions protrude outwards in a bottlebrush fashion (Isas et al., 2015; Lin et al.,

165   2017). However, our data does not allow resolving the molecular organization of the fibril core, possibly

166   due to its structural heterogeneity (Hoop et al., 2016; Lin et al., 2017).

167   Wild type Htt is known to interact with cellular membranes (Kegel-Gleason, 2013), and fibrils of polyQ-

168   expanded Htt exon 1 and other amyloids cause membrane disruption in vitro (Milanesi et al., 2012; Pieri

169   et al., 2012). Our results suggest that a cytopathological consequence of these phenomena is that Htt

170   exon 1 IB fibrils impinge on and disrupt cellular endomembranes, most prominently those of the ER. As a

171   result, IBs drive a reorganization of the ER network in their periphery. Fibril-membrane interactions are

172   thought to be largely lipid-mediated (Burke et al., 2013; Kegel et al., 2005; Trevino et al., 2012), and

173   whether any specificity for ER membranes exists (Atwal et al., 2007) remains to be determined.

174   Although it is possible that oligomers dissociating from fibril ends (Carulla et al., 2005; Martins et al.,

175   2008) contribute to these effects, high concentrations of soluble Htt97Q-GFP did not disturb membrane

176   morphology in the absence of IBs. Thus, fibrils appear to be necessary for membrane deformation.

177   The region of the ER surrounding the IBs was dramatically reduced in membrane dynamics, suggesting

178   that a wide variety of cellular processes that depend on the dynamic behavior of the ER (Zhang and Hu,

179   2016) might also be affected. Moreover, translation is halted in these regions, as ER membranes

180   contacting fibrils lacked ribosomes and the Sec61 translocon. The accumulation of ERAD factors and ER

181   chaperones suggests that cytosolic IBs locally induce misfolding of ER luminal proteins causing ER stress.

182   These results are consistent with previous findings that polyQ expression compromises ER function by

183   perturbing ERAD, ER Ca^{2+} signaling and the ER redox state, leading to ER stress in cellular and animal

184   models (Duennwald and Lindquist, 2008; Higo et al., 2010; Jiang et al., 2016; Kirstein et al., 2015;

185   Kouroku et al., 2002; Lajoie and Snapp, 2011; Leitman et al., 2013b; Tang et al., 2003). ER stress markers

186   are upregulated in Htt knock-in mice and HD patients, and alleviating ER stress is beneficial in various HD

187   models (Carnemolla et al., 2009; Lee et al., 2012; Leitman et al., 2014; Vidal et al., 2012). Thus, beyond

188   the toxic role of oligomeric aggregate species, our data suggest that the formation of large fibrillar IBs

189   (Benn et al., 2005; Liu et al., 2015; Ramdzan et al., 2017; Woerner et al., 2016) is also deleterious to the

190   cell.

191

192

199

200 **Author contributions:** F. J. B. performed all electron and light microscopy experiments, analyzed the

201 data and prepared figures. I. S. and A. M. performed cell culture experiments. M. K. and A. M.-S.

202 contributed to the computational analysis of cryo-ET data. R. K., I. D., M. S. H., F.-U. H., W. B. and R. F.-B.

203 designed research. I. D., M. S. H. and R. F.-B. supervised experiments. M. S. H., F.-U. H., W. B. and R. F.-B.

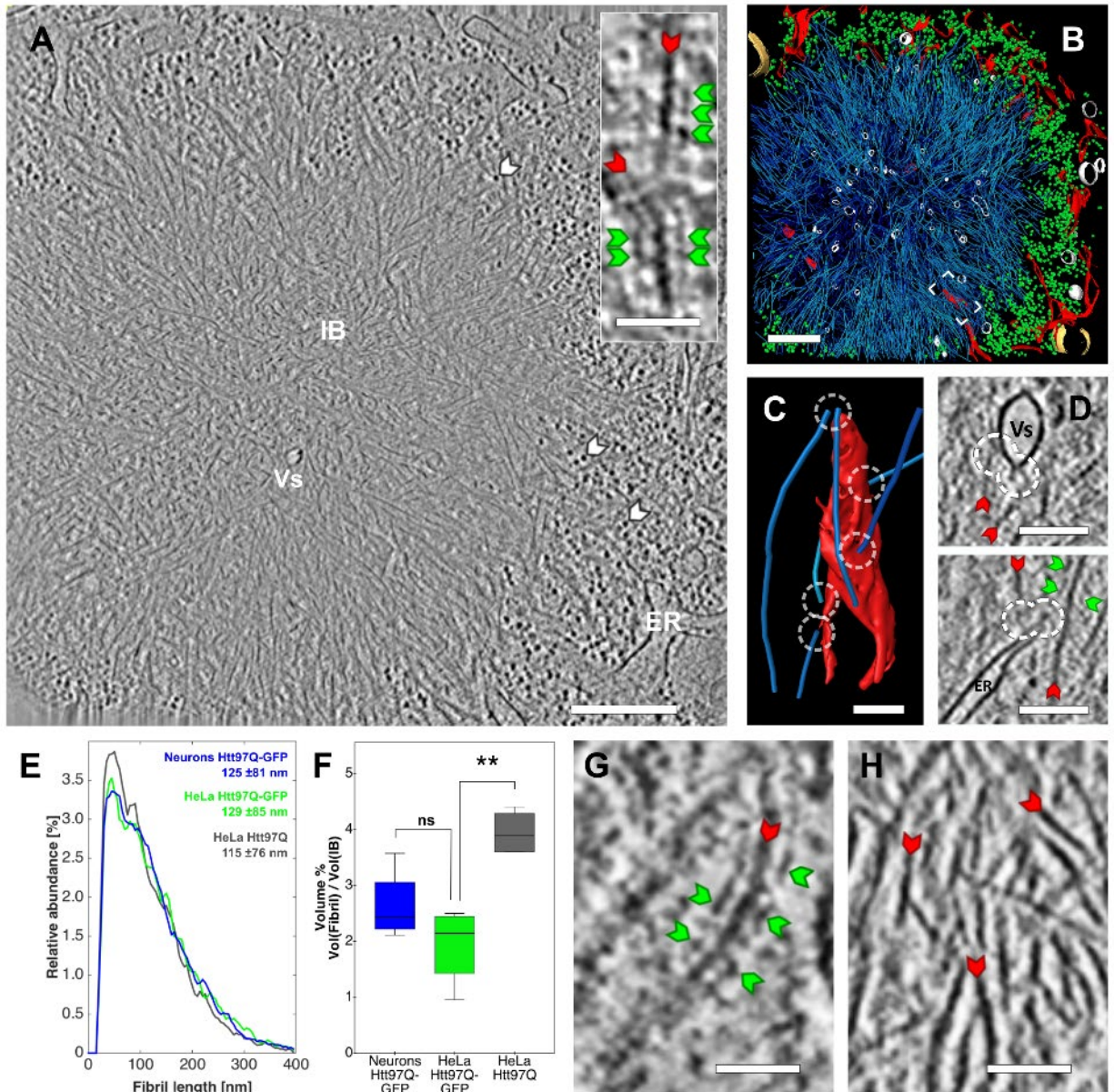204 wrote the manuscript with contributions from the other authors.

205
206

207

208

209

210

Figure 1

Fig. 1: Cytosolic IBs of Htt97Q-GFP contain amyloid-like fibrils. (**A**) Tomographic slice of an IB in an

Htt97Q-GFP-transfected mouse primary neuron. The cytoplasmic electron dense particles represent

ribosomes (white arrowheads). ER, endoplasmic reticulum; Vs, vesicle. **Inset**: high magnification image

of an Htt97Q-GFP fibril (red arrowheads) decorated by globular densities (green arrowheads). (**B**) 3D

rendering of the tomogram shown in (A). ER membranes (red), Htt97Q-GFP fibrils (cyan), ribosomes

(green), vesicles (white), mitochondria (gold). Note that the core of the IB is largely devoid of ribosomes,

218 which accumulate at the IB periphery. Scale bars: 400 nm in (A) and (B), 30 nm in (A, inset). (**C**)

219 Magnified rendering of the region marked in (B) showing interaction sites (white circles) between the

220 sides and the ends of Htt97Q-GFP fibrils and the ER membrane. Scale bar, 50 nm. (**D**) Magnified

221 tomographic slices showing Htt97Q-GFP fibrils (red arrowheads) decorated by globular densities (green

222 arrowheads) interacting with cellular membranes in Htt97Q-GFP transfected neurons. Scale bars, 100

223 nm. (**E**) Histograms of fibril length in mouse neurons expressing Htt97Q-GFP (blue), HeLa cells expressing

224 Htt97Q-GFP (green) and HeLa cells expressing Htt97Q (grey) (number of fibrils: N = 11,481, neurons;

225 Htt97Q-GFP; N = 7,648, HeLa; Htt97Q-GFP; N = 12,465, HeLa; Htt97Q; 4 tomograms for all conditions).

226 (**F**) Percentage of IB volume occupied by fibrils. ** indicates $p < 0.01$; ns, not significant in an ANOVA

227 analysis with Bonferroni post-hoc-test. (**G**) Magnified tomographic slice of an Htt97Q-GFP-transfected

228 HeLa cell showing Htt97Q-GFP fibrils (red arrowhead) decorated by globular densities (green

229 arrowheads). (**H**) Magnified tomographic slice of an Htt97Q-transfected HeLa cell showing Htt97Q fibrils.

230 Scale bars, 50 nm in (G, H). Tomographic slices are 2.8 nm (A, D) or 1.7 nm (G, H) thick. The number of

231 experiments and cells analyzed per condition is shown in Table 1.

232

Figure 2

233
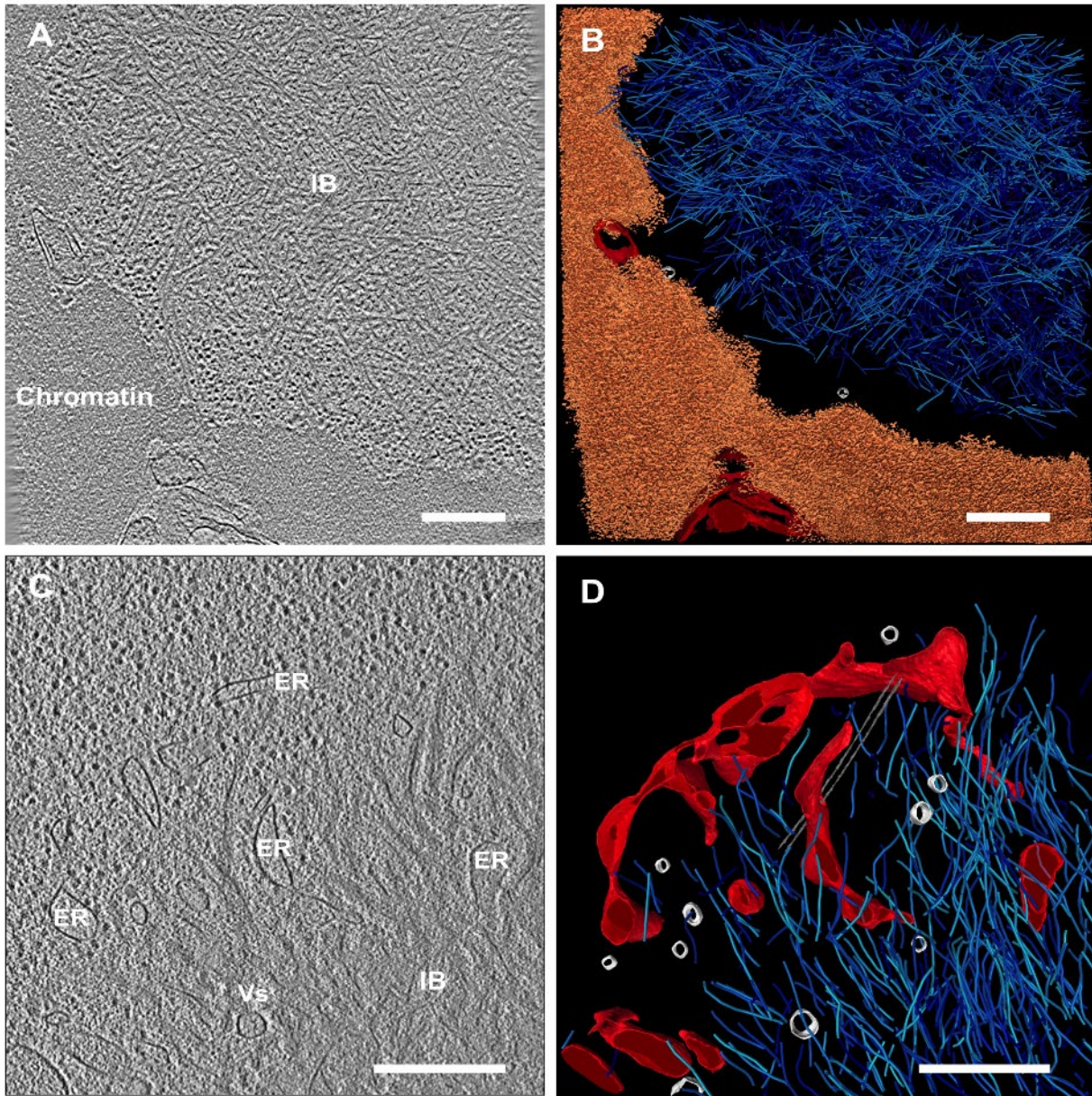
**Fig. 2: Nuclear Htt97Q-GFP IBs in neurons and cytosolic Htt64Q-GFP IBs in HeLa cells.** (**a**) 1.7 nm thick

tomographic slice of a nuclear IB in an Htt97Q-GFP-transfected neuron. Scale bars, 400 nm. (**b**) 3D

rendering respectively corresponding to (a). Chromatin (orange), nuclear envelope membranes (red),

vesicles in the periphery of the IB (white), Htt97Q-GFP fibrils (cyan). (**c**) 2.5 nm thick tomographic slice

showing an IB in an Htt64Q-GFP-transfected HeLa cell. (**d**) 3D rendering of the tomogram shown in (c).

ER membranes (red), Htt64Q-GFP fibrils (cyan), microtubule (grey parallel lines). Scale bars, 250 nm.

Figure 3
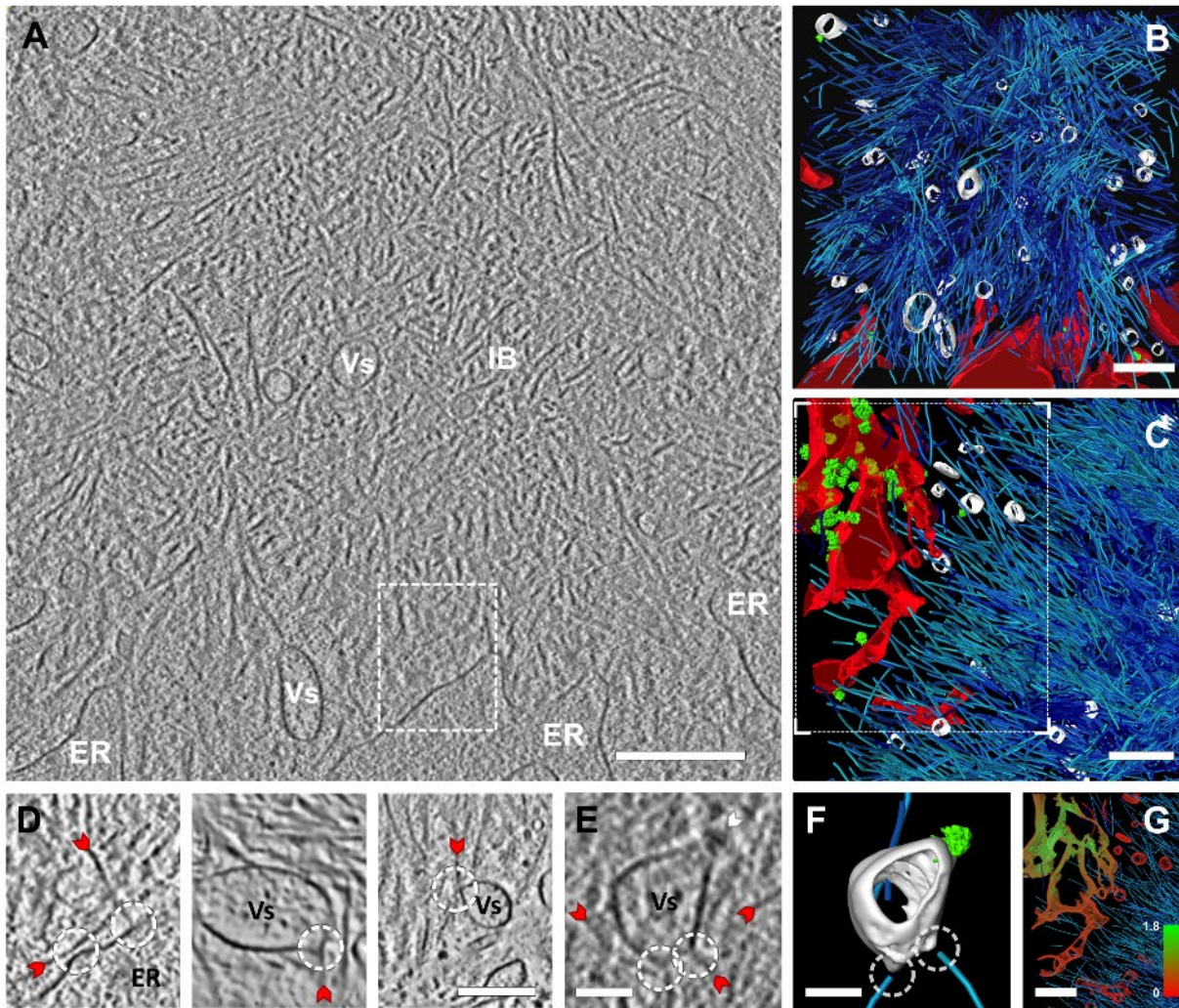
240
241

242 **Fig. 3: Htt97Q IBs interact with cellular membranes.** (**A**) Tomographic slice from the interaction zone

243 between an IB and cellular membranes in an Htt97Q-transfected HeLa cell. ER, endoplasmic reticulum;

244 IB, Htt97Q inclusion body; Vs, vesicles. (**B**) 3D rendering of the tomogram shown in (A). ER membranes

245 (red), ER-bound ribosomes (green), Htt97Q fibrils (cyan), vesicles inside the IB (white). (**C**) 3D rendering

246 of ER membranes and ER-bound ribosomes in the vicinity of Htt97Q fibrils. Note that ER-bound

247 ribosomes are depleted from ER membranes directly interacting with Htt97Q fibrils but are abundant in

248 more distal areas (see also (G)). Scale bars: 250 nm in (A-C). (**D**) Magnified tomographic slices showing

249 the sides and ends of Htt97Q (left and middle) and Htt97Q-GFP (right) fibrils (red arrowheads)

250   interacting with cellular membranes (white circles). The left panel shows the area boxed in (A) in a

251   different tomographic slice. (**E**) Magnified tomographic slice of a putative membrane-bound ribosome

252   (white arrowhead) on a small vesicle contacted (white circles) by the Htt97Q-GFP fibrils of an IB. (**F**) 3D

253   rendering of the vesicle shown in (E). Note the high curvature of the vesicle membrane at the sites of

254   interaction with fibrils. Scale bars, 100 nm in (D, E, F). (**G**) Visualization of the density of membrane-

255   bound ribosomes in the area boxed in (C). Ribosome density is indicated by color and is lower (red) on

256   ER membranes in direct contact with fibrils. Scale bar 250 nm. Tomographic slices are 1.7 nm thick. The

257   number of experiments and cells analyzed per condition is shown in Table 1.

258

Figure 4
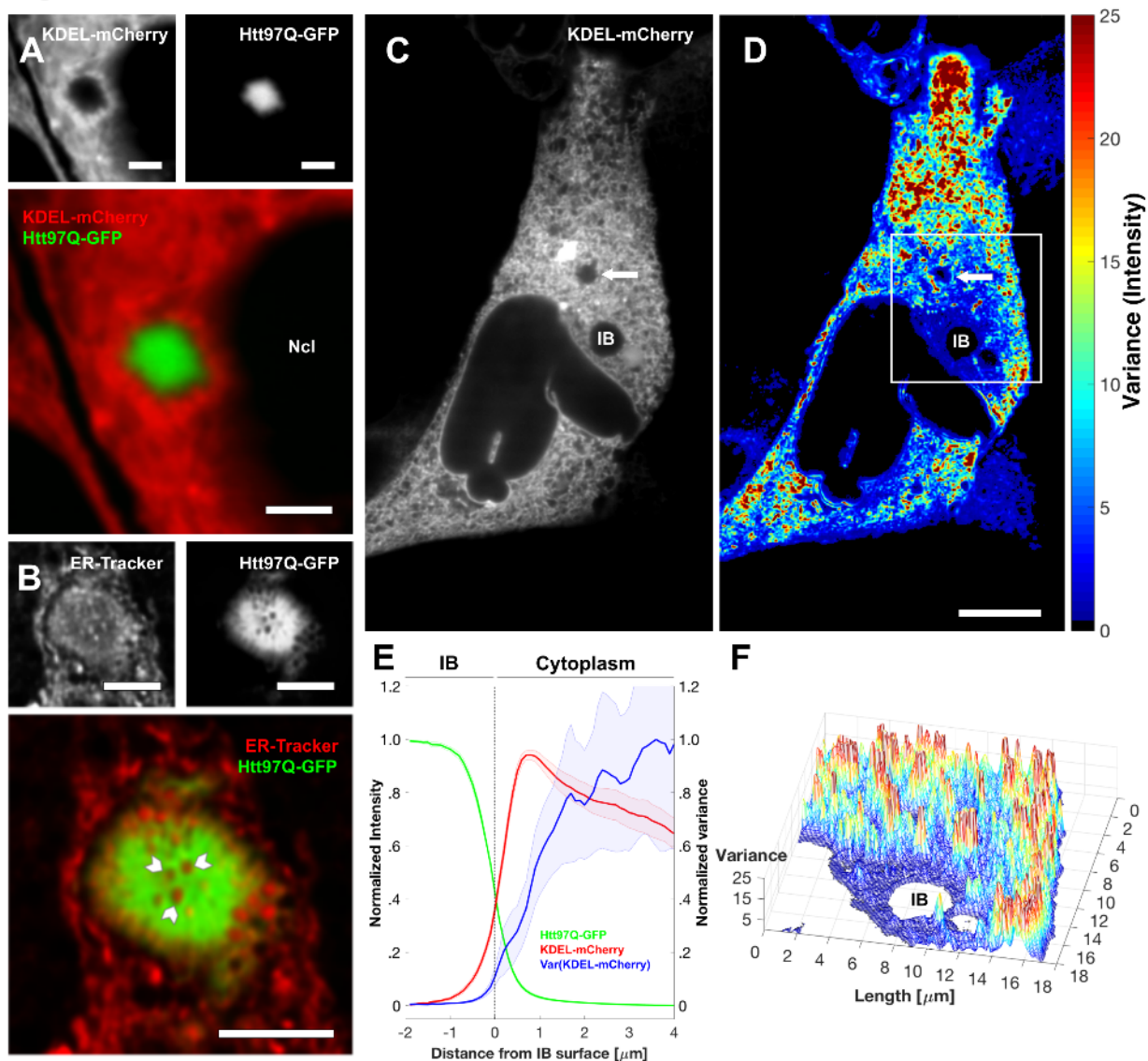
261 **Fig. 4: Htt97Q-GFP IBs locally alter ER organization and dynamics.** (**A**) HeLa cell co-expressing Htt97Q-

262 GFP (green) and the ER luminal marker KDEL-mCherry (red). Note the accumulation of ER around the IB.

263 Ncl: nucleus. (**B**) HeLa cell expressing Htt97Q-GFP (green) and labelled with ER-Tracker (red). White

264 arrowheads mark ER-positive structures inside the IB. (**C**) Additional example of a HeLa cell co-

265 expressing Htt97Q-GFP and KDEL-mCherry. A white arrow points to an Htt97Q-GFP-negative large

266 cytoplasmic structure around which ER dynamics are normal. (**D**) ER dynamics of the cell shown in (C)

267 quantified as the variance of KDEL-mCherry pixel intensity over time for 20 s. (**E**) Quantification of ER

268   membrane dynamics in the vicinity of Htt97Q-GFP IBs (N = 44 cells). Note the substantial accumulation

269   of ER (red curve; radial average of KDEL-mCherry pixel intensity) at the IB periphery (x = 0). Membrane

270   dynamics, assessed by the variance of KDEL-mCherry pixel intensity over time (blue curve), were

271   markedly slower in this ER domain than in more distal regions. Radial averages (solid lines) and 95%

272   confidence intervals (shaded areas) are shown. See Fig. S 4F-H for individual traces. (**F**) 3D

273   representation of the boxed region in (D) around the IB. Scale bars, 5 μm in (A, B), 10 μm in (C, D).

274

275 **STAR methods**

276 **Plasmids and antibodies.** The plasmids expressing myc-tagged Htt25Q exon 1-GFP, Htt64Q exon 1-GFP,

277 Htt97Q exon 1 and Htt97Q exon 1-GFP have been described previously [46,] (Bence et al., 2001; Holmberg

278 et al., 2004). The plasmid expressing mCherry-Ubiquitin was a kind gift from Eric J. Bennett & Ron R.

279 Kopito. To generate the KDEL-mCherry construct (kind gift from Lisa Vincenz-Donnelly), the signal

280 peptide of human pulmonary surfactant-associated protein B (MAESHLLQWLLLLLPTLCGPGTA) followed

281 by one alanine residue and a myc tag was fused upstream to mCherry by PCR amplification. A C-terminal

282 KDEL sequence, as well as a 5' BamH1 and a 3' Not1 digestion site were also added by PCR amplification.

283 The purified PCR product was then inserted into the pcDNA3.1+ plasmid via BamH1/Not1.

284 The following primary antibodies were used for immunofluorescence: BiP (AbCam ab21685), calnexin

285 (AbCam ab10286), calreticulin (AbCam ab14234), giantin (AbCam ab24586), p97/VCP (Cell Signalling

286 2468), PDIA6 (AbCam ab154820), Sec61A (AbCam ab183046), SEL1L (Sigma S3699) and SPFH2/ERLIN2

287 (AbCam ab128924). The following secondary antibodies were used: Anti-Rabbit Cy3 (Dianova 111-165-

288 045), Anti-Mouse Cy3 (Jackson Immunoresearch 115-165-062) and Anti-Chicken Alexa Fluor 633

289 conjugate (Thermo Fisher A21103).

290 **Cell culture.** HeLa cells (freshly obtained from ATCC; no unusual DAPI staining was observed indicating

291 no mycoplasma contamination) were seeded on holey carbon-coated 200 mesh gold EM grids

292 (Quantifoil Micro Tools, Jena, Germany) in ibidi μ-slides (ibidi, Munich) containing Dulbecco's MEM

293 (Biochrom) supplemented with 10% fetal bovine serum, 2mM L-Glutamine, 100 Units/mL penicillin,

294 100μg/mL streptomycin and non-essential amino acids cocktail (Gibco) and cultured at 37°C with 10%

295 CO_2. The cells were transfected by lipofection using Lipofectamine 2000 (Invitrogen) with either Htt25Q-

296 GFP, Htt64Q-GFP, Htt97Q-GFP or Htt97Q together with mCherry-ubiquitin as per manufacturer's

297 protocol. In co-transfected cells mCherry-ubiquitin formed a ring around mHtt inclusion bodies (IBs) that

298 facilitated correlative microscopy [21]. 30 min prior to imaging the cells were stained with AnnexinV

299   conjugated to Alexa Fluor 594 (LifeTechnologies) to exclude cells undergoing apoptosis from further

300   analysis.

301   **Hippocampal neuron culture and transfection.** Holey carbon-coated 200 mesh gold EM grids were

302   sterilized in ethanol for 10 min, washed several times in double distilled water and transferred to culture

303   dishes containing water. Grids and dishes were coated with poly-D-lysine (1 mg/ml in borate buffer) and

304   laminin (7.5 µg/ml in PBS) for 24 h each, washed with PBS three times and placed in neurobasal medium

305   supplemented with B27 containing 0.5 mM Glutamine (all reagents from Thermo Fisher). During washes

306   and medium exchange steps, grids were transferred into another dish containing appropriate liquid to

307   prevent grids from drying.

308   Hippocampi from embryonic day 17 mice (C57BL/6N, either sex) were separated from diencephalic

309   structures and digested individually with 0.25% trypsin containing 1 mM 2,2',2'',2'''-(ethane-1,2-

310   diyldinitrilo) tetraacetic acid (EDTA) for 20 min at 37°C. Neurons were plated in 24-well plates (60,000

311   per well) on the coated grids. After 6 days in culture at 37°C in 5% CO_2, neurons were transfected with

312   Htt97Q-GFP using DNA-In^{TM} *Neuro* (GlobalStem) according to the manufacturer's protocol.

313   **Immunofluorescence.** HeLa cells were seeded on poly-L-lysine coated glass coverslips (NeuVitro),

314   transfected with Htt97Q-GFP and fixed 24-48 h post-transfection using 4% paraformaldehyde in PBS for

315   10 min, permeabilized with 0.1% (v/v) Triton X-100 in PBS for 5 min and blocked in 5% milk in PBS for 1 h

316   at room temperature. The cells were then washed and primary antibodies were applied overnight at a

317   dilution of 1:500 to 1:1000 in blocking solution at 4°C, washed in PBS and incubated with secondary

318   antibodies at a dilution of 1:5000 in PBS at room temperature for 1-2 h. Coverslips were stained with

319   500 nM DAPI in PBS for 5 min, washed several times with PBS and mounted in fluorescence mounting

320   medium (Dako).

321 To investigate the identity of the membranous structures contained inside IBs, HeLa cells were transfected

322 with Htt97Q-GFP and loaded with either ER-Tracker Red or Mito-Tracker Red (Thermo Fischer) 24h after

323 transfection. The cells were subsequently fixed and imaged as described below.

324 **Correlative light microscopy and live cell imaging.** To locate cells containing mHtt IBs and suitable for

325 cryo-ET, cells were imaged in an atmosphere of 37°C and 10% CO_2 using a CorrSight light microscope

326 (FEI, Hillsboro, USA) equipped with bright field and spinning disc confocal laser illumination

327 (405/488/561/640 nm), 20x (air, NA 0.8) and 63x (oil, NA 1.4) Plan Achromat objectives (Carl Zeiss, Jena,

328 Germany) and a 1344 x 1024 pixel camera with a pixel size of 6.4 µm (Hamamatsu Digital Camera

329 C10600 ORCA-R2).

330 For correlative microscopy a map of the EM grid was acquired with 20x magnification (object pixel size

331 323 nm) in spinning disc confocal mode. Htt97Q and Htt97Q-GFP-expressing HeLa cells and primary

332 neurons were imaged 24 h after transfection, as this yielded the best compromise between cell death

333 and formation of IB. Protein expression was allowed for 48-72h in Htt64Q-GFP-expressing HeLa cells, as

334 IB formation was slower.

335 For investigation of ER dynamics, HeLa cells were co-transfected with Htt97Q-GFP and KDEL-mCherry and

336 imaged at 5-10 Hz with 63x magnification (object pixel size 102 nm) in spinning disk confocal mode for 20-

337 30 s. The z slice containing the maximum IB diameter was analyzed further for each movie. Movies were

338 first bleach-corrected using the exponential fit tool of Fiji (Schindelin et al., 2012) and further processed

339 using in-house Matlab (MathWorks) scripts. The IB boundary (x = 0 in Fig. 4E and Fig. S 3F-H) was

340 estimated as the line where Htt97Q-GFP intensity dropped to 40 % of its maximum value in each IB. A

341 radial average of KDEL-mCherry pixel intensity was calculated from this mask within the cytoplasm. The

342 radial variance of KDEL-mCherry pixel intensity was calculated over time, and normalized by pixel intensity

343 to account for different KDEL-mCherry expression levels in different cells. The maximum of the curve was

344   scaled to 1. The normalized variance was used as readout for ER membrane dynamics (blue curves in Fig.

345   4E and Fig. S 3H).

346   **Cell vitrification.** After light microscopy the cells were incubated for 1-5 min in DMEM containing 10%

347   glycerol as a cryo-protectant to ensure full vitrification. The grids were then mounted on a manual

348   plunger, blotted from the back side using Whatmann paper #1 and plunged into a 2:1 ethane:propane

349   mixture cooled down to liquid nitrogen temperature.

350   **Cryo-focused ion beam milling.** To prepare thin electron transparent lamellae containing mHtt IBs and

351   surrounding cellular structures, plunge-frozen grids were first mounted into Autogrid frames (FEI).

352   Autogrids were mounted into a dual-beam Quanta 3D focused ion beam (FIB) / scanning electron

353   microscope (SEM) (FEI) using a custom-built transfer shuttle and a cryo-transfer system (PP3000T,

354   Quorum). The samples were kept at -180° C throughout FIB milling by the microscope's cryo-stage. To

355   target cells containing IBs an overview map of the EM grid was acquired by SEM at 10 kV at 100x

356   magnification (object pixel size 1.1 μm) and correlated with the light microscopy map using MAPS

357   software (FEI). Thereby, the fluorescence signal was overlaid on the correlated SEM micrograph. For

358   Htt97Q/mCherry-ubiquitin co-transfected cells a custom-made Matlab algorithm was applied to the

359   correlated light microscopy/SEM image to select IBs as ring-shaped structures and classify them

360   according to their size and usability in terms of distance to the grid bars. To protect the milling front of

361   the lamellae, gaseous organic platinum was frozen on top of the grid using a gas injection system. 15-30

362   μm wide lamellae were prepared in target cells using a Ga^+ ion beam at 30 kV at shallow angles (8-14°)

363   in four consecutive steps: initially cells were abrased in 500 nm steps from the top down with 500-1000

364   pA and imaged consecutively by SEM at 2.5 kV, 4.1 pA in integration mode to identify IBs. Further

365   rectangular patterns were defined above and below the intended lamella with 2 μm spacing for the

366   rough milling step (ion beam current of 500-1000 pA), followed by fine milling with 800 nm spacing (200

367   pA) and a final polishing step down to the final lamella thickness of 150-250 nm (50 pA). To reduce

368   lamella charging during phase plate cryo-ET data acquisition a thin layer of pure metallic Pt was

369   sputtered onto the lamella under cryo conditions at the PP3000T transfer system with the following

370   parameters [10]: 5 mA sputtering current, 500 V between stage and sputtering target and 10 s of exposure

371   at 4.5×10^{-2} mbar.

372   **Cryo-electron tomography.** Cryo-FIB lamellas were imaged using a Titan cryo-transmission electron

373   microscope (TEM) (FEI) equipped with a field emission gun operated at 300 kV, a Volta phase plate [3], a

374   post-column energy filter (Gatan, Pleasanton, CA, USA) operated at zero-loss and a K2 Summit direct

375   electron detector (Gatan). Low magnification images of lamellas were recorded at 11.500 x (object pixel

376   size 1.312 nm) and stitched using ICE (Microsoft Research) to produce complete lamella overviews.

377   Phase plate alignment and operation was carried out as described (Fukuda et al., 2015). Upon phase

378   plate conditioning, high magnification (19,500x, object pixel size 0.710 nm for Fig. 2A; 33,000x, object

379   pixel size 0.421 nm for all other tomograms) tilt series were recorded at locations of interest using the

380   SerialEM (Mastronarde, 2005) low dose acquisition scheme with a tilt increment of 2°, typically spanning

381   an angular range from -52° to 70°. Target defocus was set to -0.5 µm. The K2 camera was operated in

382   dose fractionation mode recording frames every 0.2 s. For each tilt series, a new spot on the phase plate

383   was selected. The total dose was limited to 70-150 $e^{-}/Å^{2}$.

384   **Tomogram reconstruction and analysis.** Raw K2 camera frames were aligned using an in-house

385   software following previously developed procedures (Qiang et al., 2013). The resulting tilt series were

386   aligned using the patch tracking option of the IMOD package (Kremer et al., 1996) and reconstructed by

387   weighted back projection. After reconstruction, the tilt series were cleaned of surface contamination

388   (ice crystals and sputtered metallic Pt) using the MaskTomRec software (Fernandez et al., 2016), re-

389   aligned and reconstructed again.

390   Membranes were automatically segmented using the TomoSegMemTV package (Martinez-Sanchez et

391   al., 2014) and refined manually when necessary using Amira (FEI Visualization Sciences Group). mHtt

392   fibrils were automatically detected using the XTracing Module in Amira (Rigort et al., 2012b). In brief,

393   tomograms were denoised by a non-local means filter and searched for a cylindrical template of 8 nm in

394   diameter and 42 nm in length. The resulting cross-correlation fields were thresholded at an empirical

395   value of 0.68-0.72 that produced optimal numbers of true positives and negatives. The thresholded

396   correlation fields were used as starting point for the filament tracing process. The length and orientation

397   distribution of the resulting fibrils was then measured. The total volume occupied by fibrils was

398   calculated by multiplying the total length of all fibrils by πr^2, where r is the radius of the fibrils, here 4

399   nm. The fraction of IB occupied by fibrils was determined by diving the total fibril volume by the volume

400   of a manually traced envelope of the IB.

401   **Persistence length analysis.** The persistence length (L_P) was determined using an in-house script. L_P is a

402   measure of the stiffness of polymers that can be defined as the average distance for which a filament is

403   not bent. It is calculated as the expectation value of cos θ, where θ is the angle between two tangents to

404   the fibril at positions 0 and l (Nagashima and Asakura, 1980):

405    $$\langle \cos(\theta_0 - \theta_l) \rangle = e^{-\left(l/L_p\right)}$$

406   Intuitively, the larger θ (i.e. the smaller L_P) the more flexible is the fibril.

407   The Young's modulus E defines the relation between applied force and deformation of the fibril and can

408   be calculated from L_P as:

409    $$E = \frac{L_P k_B T}{I}$$

410   where k_B is the Boltzmann constant (1.38×10^{-23} m^2 kg s^{-2} K^{-1}), T is the absolute temperature (here 295 K)

411   and I is the momentum of inertia, which for a solid rod can be calculated from its radius r as:

412    $$I = \frac{\pi r^4}{4}$$

413   The force necessary to deform the cell membrane into filopodia-like extensions or to drive membrane

414   fission by dynamin has been estimated in the order of 20 pN [34], which would result in only a 1 % axial

415   deformation of an Htt97Q fibril according to:

416
$$E = \frac{\sigma(\varepsilon)}{\varepsilon} = \frac{F/A_0}{\Delta L/L_0}$$

417   where σ is the stress applied (force F divided by the cross section of the fibril A_0) and ε the resulting

418   strain or deformation (the increase in length ΔL divided by the initial length L_0). Therefore, we conclude

419   that Htt97Q fibrils could easily withstand or exert the forces necessary to deform cellular membranes

420   without rupturing.

421   **Ribosome template matching and calculation of ER-bound ribosome density.** ER-bound ribosomes

422   were analyzed by template matching using PyTom and TOM software (Hrabe et al., 2012). In brief,

423   tomograms were searched for the structure of a membrane-bound ribosome (Pfeffer et al., 2012)

424   (Electron Microscopy Data Bank, EMDB, accession number 2099) downsampled to 40 Å resolution in a

425   volume limited to < 100 nm distance from previously segmented ER membranes. The top cross-

426   correlation hits were screened visually and further filtered to discard ribosomes whose center was

427   located more than 18 nm away from the ER membrane. The remaining particles were aligned by real

428   space alignment and classified into six groups using constrained principle component analysis and k-

429   means clustering. One of those classes yielded non-membrane bound ribosomes and was discarded,

430   whereas the others contained mainly true positives and were pooled.

431   Each membrane-bound ribosome center coordinate was mapped to a central voxel on the membrane

432   plane of the ribosome template and overlapped with the membrane segmentation using in-house

433   Matlab scripts to discard particles with wrong orientation. The membrane segmentation was

434   transformed into a graph (Deo, 2016) using the graph-tool python library (Peixoto) as follows: All voxels

435   of the ER or vesicle membranes were added to the set of vertices. All pairs of vertices representing

436   neighboring voxels were connected by edges, resulting in a fully-connected graph. The shortest

437   distances via the membrane (geodesic distance) from each membrane voxel to the ribosome center

438   voxels on the membrane (d) were calculated using the graph-tool python library. The ribosome density

439   (D) for each membrane voxel was defined as:

440 $$D = \sum_{(reachable\ ribosomes)} \frac{1}{d + 1}$$

441   Thus, for every membrane voxel, the higher the number of reachable ribosomes and the shorter the

442   distances to them, the higher D value.

443   The cytosolic ribosomes shown in Fig. 1 B were detected by template matching using the structure of a

444   cytosolic ribosome (EMDB accession number 5592).

445   **Determination of ER membrane curvature.** First, ER membrane segmentations were pre-processed with

446   morphological operations to remove small holes. Afterwards, they were transformed into a signed,

447   single-layer surface using in-house python software; this procedure was based on the Visualization

448   Toolkit library (http://www.vtk.org) implementation of Hoppe's surface reconstruction algorithm

449   (http://hhoppe.com/proj/thesis/). A graph for recovering surface mesh topology was then constructed

450   using the graph-tool python library, so that every vertex represents a triangle center, and every edge

451   connects two adjacent triangles. The graph was used to clean the most of the artifacts generated by the

452   surface reconstruction procedure: 3 pixel-wide surface borders as well as small (below 100 triangles)

453   disconnected components were removed.

454   Local surface curvature information is described by the estimation of maximal and minimal principal

455   curvatures (κ_1 and κ_2 respectively) of an in-house implementation of the normal vector voting algorithm

456   (Page et al., 2002). The graph surface representation was used to measure geodesic distances between

457   triangles by approximating them to shortest paths along graph edges. For each surface triangle, surface

458   triangles with centers falling within 9 nm from its center were considered as the local neighborhood for

459   the normal vector voting procedure. To represent surface deformation with a single scalar value for

460   every triangle, principal curvatures were combined to compute curvedness (Koenderink and van Doorn,

461   1992), defined as:

462
$$Curvedness = \sqrt{\frac{\kappa_1^2 + \kappa_2^2}{2}}$$

463   **Statistical analysis.** The number of cells analyzed for each condition is shown in Table 1. Tomograms of

464   poor technical quality or showing signs of cell death were excluded. As the fibril tracing procedure can

465   be affected by noise (Rigort et al., 2012b), for optimal tracing and subsequent analysis (fibril length,

466   density, persistence length, Young's modulus), the 4 tomograms with best signal-to-noise ratio were

467   selected for each condition. This resulted in a large number of fibrils being analyzed: N = 11,481,

468   neurons; Htt97Q-GFP; N = 7,648, HeLa; Htt97Q-GFP; N = 12,465, HeLa; Htt97Q. For the fibril density

469   analysis, statistical significance was calculated by ANOVA analysis with Bonferroni post-hoc-test. ER

470   dynamics were analyzed in 44 cells from 2 independent experiments. The analysis included all cells in

471   which IB size was in the range of that observed by cryo-ET, which was the case for the large majority of

472   IB-containing cells.

473
474

References

Arrasate, M., and Finkbeiner, S. (2012). Protein aggregates in Huntington's disease. Exp Neurol *238*, 1-11.

Asano, S., Fukuda, Y., Beck, F., Aufderheide, A., Forster, F., Danev, R., and Baumeister, W. (2015). A molecular census of 26S proteasomes in intact neurons. Science *347*, 439-442.

Atwal, R.S., Xia, J., Pinchev, D., Taylor, J., Epand, R.M., and Truant, R. (2007). Huntingtin has a membrane association signal that can modulate huntingtin aggregation, nuclear entry and toxicity. Hum Mol Genet *16*, 2600-2615.

Bence, N.F., Sampat, R.M., and Kopito, R.R. (2001). Impairment of the ubiquitin-proteasome system by protein aggregation. Science *292*, 1552-1555.

Benn, C.L., Landles, C., Li, H., Strand, A.D., Woodman, B., Sathasivam, K., Li, S.H., Ghazi-Noori, S., Hockly, E., Faruque, S.M.*, et al.* (2005). Contribution of nuclear and extranuclear polyQ to neurological phenotypes in mouse models of Huntington's disease. Hum Mol Genet *14*, 3065-3078.

Bucciantini, M., Giannoni, E., Chiti, F., Baroni, F., Formigli, L., Zurdo, J., Taddei, N., Ramponi, G., Dobson, C.M., and Stefani, M. (2002). Inherent toxicity of aggregates implies a common mechanism for protein misfolding diseases. Nature *416*, 507-511.

Bugg, C.W., Isas, J.M., Fischer, T., Patterson, P.H., and Langen, R. (2012). Structural features and domain organization of huntingtin fibrils. J Biol Chem *287*, 31739-31746.

Burke, K.A., Hensal, K.M., Umbaugh, C.S., Chaibva, M., and Legleiter, J. (2013). Huntingtin disrupts lipid bilayers in a polyQ-length dependent manner. Biochim Biophys Acta *1828*, 1953-1961.

Carnemolla, A., Fossale, E., Agostoni, E., Michelazzi, S., Calligaris, R., De Maso, L., Del Sal, G., MacDonald, M.E., and Persichetti, F. (2009). Rrs1 is involved in endoplasmic reticulum stress response in Huntington disease. J Biol Chem *284*, 18167-18173.

Carulla, N., Caddy, G.L., Hall, D.R., Zurdo, J., Gairi, M., Feliz, M., Giralt, E., Robinson, C.V., and Dobson, C.M. (2005). Molecular recycling within amyloid fibrils. Nature *436*, 554-558.

Danev, R., Buijsse, B., Khoshouei, M., Plitzko, J.M., and Baumeister, W. (2014). Volta potential phase plate for in-focus phase contrast transmission electron microscopy. Proc Natl Acad Sci U S A *111*, 15635-15640.

Davies, S.W., Turmaine, M., Cozens, B.A., DiFiglia, M., Sharp, A.H., Ross, C.A., Scherzinger, E., Wanker, E.E., Mangiarini, L., and Bates, G.P. (1997). Formation of neuronal intranuclear inclusions underlies the neurological dysfunction in mice transgenic for the HD mutation. Cell *90*, 537-548.

Deo, N. (2016). Graph theory with applications to engineering and computer science (Mineola, New York: Dover publications).

DiFiglia, M., Sapp, E., Chase, K.O., Davies, S.W., Bates, G.P., Vonsattel, J.P., and Aronin, N. (1997). Aggregation of huntingtin in neuronal intranuclear inclusions and dystrophic neurites in brain. Science *277*, 1990-1993.

Duennwald, M.L., and Lindquist, S. (2008). Impaired ERAD and ER stress are early and specific events in polyglutamine toxicity. Genes Dev *22*, 3308-3319.

Fernandez, J.J., Laugks, U., Schaffer, M., Bauerlein, F.J., Khoshouei, M., Baumeister, W., and Lucic, V. (2016). Removing contamination-induced reconstruction artifacts from cryo-electron tomograms. Biophys J *110*, 850-859.

520   Finkbeiner, S. (2011). Huntington's Disease. Cold Spring Harb Perspect Biol *3*.

521   Fukuda, Y., Laugks, U., Lucic, V., Baumeister, W., and Danev, R. (2015). Electron
522   cryotomography of vitrified cells with a Volta phase plate. J Struct Biol *190*, 143-154.

523   Gu, X., Cantle, J.P., Greiner, E.R., Lee, C.Y., Barth, A.M., Gao, F., Park, C.S., Zhang, Z.,
524   Sandoval-Miller, S., Zhang, R.L.*, et al.* (2015). N17 Modifies mutant Huntingtin nuclear
525   pathogenesis and severity of disease in HD BAC transgenic mice. Neuron *85*, 726-741.

526   Gu, X., Greiner, E.R., Mishra, R., Kodali, R., Osmand, A., Finkbeiner, S., Steffan, J.S.,
527   Thompson, L.M., Wetzel, R., and Yang, X.W. (2009). Serines 13 and 16 are critical
528   determinants of full-length human mutant huntingtin induced disease pathogenesis in HD mice.
529   Neuron *64*, 828-840.

530   Haass, C., and Selkoe, D.J. (2007). Soluble protein oligomers in neurodegeneration: lessons from
531   the Alzheimer's amyloid beta-peptide. Nat Rev Mol Cell Biol *8*, 101-112.

532   Higo, T., Hamada, K., Hisatsune, C., Nukina, N., Hashikawa, T., Hattori, M., Nakamura, T., and
533   Mikoshiba, K. (2010). Mechanism of ER stress-induced brain damage by IP(3) receptor. Neuron
534   *68*, 865-878.

535   Hipp, M.S., Park, S.H., and Hartl, F.U. (2014). Proteostasis impairment in protein-misfolding
536   and -aggregation diseases. Trends Cell Biol *24*, 506-514.

537   Hipp, M.S., Patel, C.N., Bersuker, K., Riley, B.E., Kaiser, S.E., Shaler, T.A., Brandeis, M., and
538   Kopito, R.R. (2012). Indirect inhibition of 26S proteasome activity in a cellular model of
539   Huntington's disease. J Cell Biol *196*, 573-587.

540   Holmberg, C.I., Staniszewski, K.E., Mensah, K.N., Matouschek, A., and Morimoto, R.I. (2004).
541   Inefficient degradation of truncated polyglutamine proteins by the proteasome. EMBO J *23*,
542   4307-4318.

543   Hoop, C.L., Lin, H.K., Kar, K., Magyarfalvi, G., Lamley, J.M., Boatz, J.C., Mandal, A.,
544   Lewandowski, J.R., Wetzel, R., and van der Wel, P.C. (2016). Huntingtin exon 1 fibrils feature
545   an interdigitated beta-hairpin-based polyglutamine core. Proc Natl Acad Sci U S A *113*, 1546-
546   1551.

547   Hrabe, T., Chen, Y., Pfeffer, S., Cuellar, L.K., Mangold, A.V., and Forster, F. (2012). PyTom: a
548   python-based toolbox for localization of macromolecules in cryo-electron tomograms and
549   subtomogram analysis. J Struct Biol *178*, 177-188.

550   Isas, J.M., Langen, R., and Siemer, A.B. (2015). Solid-state nuclear magnetic resonance on the
551   static and dynamic domains of huntingtin exon-1 fibrils. Biochemistry *54*, 3942-3949.

552   Jiang, Y., Chadwick, S.R., and Lajoie, P. (2016). Endoplasmic reticulum stress: The cause and
553   solution to Huntington's disease? Brain Res *1648*, 650-657.

554   Kawai-Noma, S., Pack, C.G., Kojidani, T., Asakawa, H., Hiraoka, Y., Kinjo, M., Haraguchi, T.,
555   Taguchi, H., and Hirata, A. (2010). In vivo evidence for the fibrillar structures of Sup35 prions in
556   yeast cells. J Cell Biol *190*, 223-231.

557   Kegel-Gleason, K.B. (2013). Huntingtin interactions with membrane phospholipids: strategic
558   targets for therapeutic intervention? J Huntingtons Dis *2*, 239-250.

559   Kegel, K.B., Sapp, E., Yoder, J., Cuiffo, B., Sobin, L., Kim, Y.J., Qin, Z.H., Hayden, M.R.,
560   Aronin, N., Scott, D.L.*, et al.* (2005). Huntingtin associates with acidic phospholipids at the
561   plasma membrane. J Biol Chem *280*, 36464-36473.

562   Kirstein, J., Morito, D., Kakihana, T., Sugihara, M., Minnen, A., Hipp, M.S., Nussbaum-
563   Krammer, C., Kasturi, P., Hartl, F.U., Nagata, K.*, et al.* (2015). Proteotoxic stress and ageing
564   triggers the loss of redox homeostasis across cellular compartments. EMBO J *34*, 2334-2349.

Koenderink, J.J., and van Doorn, A.J. (1992). Surface shape and curvature scales. Image Vis Comput *10*, 557-564.

Kouroku, Y., Fujita, E., Jimbo, A., Kikuchi, T., Yamagata, T., Momoi, M.Y., Kominami, E., Kuida, K., Sakamaki, K., Yonehara, S.*, et al.* (2002). Polyglutamine aggregates stimulate ER stress signals and caspase-12 activation. Hum Mol Genet *11*, 1505-1515.

Kremer, J.R., Mastronarde, D.N., and McIntosh, J.R. (1996). Computer visualization of three-dimensional image data using IMOD. J Struct Biol *116*, 71-76.

Lajoie, P., and Snapp, E.L. (2011). Changes in BiP availability reveal hypersensitivity to acute endoplasmic reticulum stress in cells expressing mutant huntingtin. J Cell Sci *124*, 3332-3343.

Lee, H., Noh, J.Y., Oh, Y., Kim, Y., Chang, J.W., Chung, C.W., Lee, S.T., Kim, M., Ryu, H., and Jung, Y.K. (2012). IRE1 plays an essential role in ER stress-mediated aggregation of mutant huntingtin via the inhibition of autophagy flux. Hum Mol Genet *21*, 101-114.

Leitman, J., Barak, B., Benyair, R., Shenkman, M., Ashery, U., Hartl, F.U., and Lederkremer, G.Z. (2014). ER stress-induced eIF2-alpha phosphorylation underlies sensitivity of striatal neurons to pathogenic huntingtin. PLoS One *9*, e90803.

Leitman, J., Ron, E., Ogen-Shtern, N., and Lederkremer, G.Z. (2013a). Compartmentalization of endoplasmic reticulum quality control and ER-associated degradation factors. DNA Cell Biol *32*, 2-7.

Leitman, J., Ulrich Hartl, F., and Lederkremer, G.Z. (2013b). Soluble forms of polyQ-expanded huntingtin rather than large aggregates cause endoplasmic reticulum stress. Nat Commun *4*, 2753.

Lin, H.K., Boatz, J.C., Krabbendam, I.E., Kodali, R., Hou, Z., Wetzel, R., Dolga, A.M., Poirier, M.A., and van der Wel, P.C.A. (2017). Fibril polymorphism affects immobilized non-amyloid flanking domains of huntingtin exon1 rather than its polyglutamine core. Nat Commun *8*, 15462.

Liu, K.Y., Shyu, Y.C., Barbaro, B.A., Lin, Y.T., Chern, Y., Thompson, L.M., James Shen, C.K., and Marsh, J.L. (2015). Disruption of the nuclear membrane by perinuclear inclusions of mutant huntingtin causes cell-cycle re-entry and striatal cell death in mouse and cell models of Huntington's disease. Hum Mol Genet *24*, 1602-1616.

Macdonald, M. (1993). A novel gene containing a trinucleotide repeat that is expanded and unstable on Huntington's disease chromosomes. Cell *72*, 971-983.

Mahamid, J., Pfeffer, S., Schaffer, M., Villa, E., Danev, R., Cuellar, L.K., Forster, F., Hyman, A.A., Plitzko, J.M., and Baumeister, W. (2016). Visualizing the molecular sociology at the HeLa cell nuclear periphery. Science *351*, 969-972.

Mangiarini, L., Sathasivam, K., Seller, M., Cozens, B., Harper, A., Hetherington, C., Lawton, M., Trottier, Y., Lehrach, H., Davies, S.W.*, et al.* (1996). Exon 1 of the HD gene with an expanded CAG repeat is sufficient to cause a progressive neurological phenotype in transgenic mice. Cell *87*, 493-506.

Martinez-Sanchez, A., Garcia, I., Asano, S., Lucic, V., and Fernandez, J.J. (2014). Robust membrane detection based on tensor voting for electron tomography. J Struct Biol *186*, 49-61.

Martins, I.C., Kuperstein, I., Wilkinson, H., Maes, E., Vanbrabant, M., Jonckheere, W., Van Gelder, P., Hartmann, D., D'Hooge, R., De Strooper, B.*, et al.* (2008). Lipids revert inert Abeta amyloid fibrils to neurotoxic protofibrils that affect learning in mice. EMBO J *27*, 224-233.

Mastronarde, D.N. (2005). Automated electron microscope tomography using robust prediction of specimen movements. J Struct Biol *152*, 36-51.

Milanesi, L., Sheynis, T., Xue, W.F., Orlova, E.V., Hellewell, A.L., Jelinek, R., Hewitt, E.W., Radford, S.E., and Saibil, H.R. (2012). Direct three-dimensional visualization of membrane disruption by amyloid fibrils. Proc Natl Acad Sci U S A *109*, 20455-20460.

Nagashima, H., and Asakura, S. (1980). Dark-field light microscopic study of the flexibility of F-actin complexes. J Mol Biol *136*, 169-182.

Olzscha, H., Schermann, S.M., Woerner, A.C., Pinkert, S., Hecht, M.H., Tartaglia, G.G., Vendruscolo, M., Hayer-Hartl, M., Hartl, F.U., and Vabulas, R.M. (2011). Amyloid-like aggregates sequester numerous metastable proteins with essential cellular functions. Cell *144*, 67-78.

Orr, H.T., and Zoghbi, H.Y. (2007). Trinucleotide repeat disorders. Annu Rev Neurosci *30*, 575-621.

Ossato, G., Digman, M.A., Aiken, C., Lukacsovich, T., Marsh, J.L., and Gratton, E. (2010). A two-step path to inclusion formation of huntingtin peptides revealed by number and brightness analysis. Biophys J *98*, 3078-3085.

Page, D.L., Sun, Y., Koschan, A.F., Paik, J., and Abidi, M.A. (2002). Normal vector voting: Crease detection and curvature estimation on large, noisy meshes. Graphical Models *64*, 199-229.

Park, S.H., Kukushkin, Y., Gupta, R., Chen, T., Konagai, A., Hipp, M.S., Hayer-Hartl, M., and Hartl, F.U. (2013). PolyQ proteins interfere with nuclear degradation of cytosolic proteins by sequestering the Sis1p chaperone. Cell *154*, 134-145.

Peixoto, T.P. (2014). The graph-tool python library.

Pfeffer, S., Brandt, F., Hrabe, T., Lang, S., Eibauer, M., Zimmermann, R., and Forster, F. (2012). Structure and 3D arrangement of endoplasmic reticulum membrane-associated ribosomes. Structure *20*, 1508-1518.

Pieri, L., Madiona, K., Bousset, L., and Melki, R. (2012). Fibrillar alpha-synuclein and huntingtin exon 1 assemblies are toxic to the cells. Biophys J *102*, 2894-2905.

Qian, S.B., Ott, D.E., Schubert, U., Bennink, J.R., and Yewdell, J.W. (2002). Fusion proteins with COOH-terminal ubiquitin are stable and maintain dual functionality in vivo. J Biol Chem *277*, 38818-38826.

Qiang, L., Fujita, R., and Abeliovich, A. (2013). Remodeling neurodegeneration: somatic cell reprogramming-based models of adult neurological disorders. Neuron *78*, 957-969.

Qin, Z.H., Wang, Y., Sapp, E., Cuiffo, B., Wanker, E., Hayden, M.R., Kegel, K.B., Aronin, N., and DiFiglia, M. (2004). Huntingtin bodies sequester vesicle-associated proteins by a polyproline-dependent interaction. J Neurosci *24*, 269-281.

Ramdzan, Y.M., Trubetskov, M.M., Ormsby, A.R., Newcombe, E.A., Sui, X., Tobin, M.J., Bongiovanni, M.N., Gras, S.L., Dewson, G., Miller, J.M.L*., et al.* (2017). Huntingtin Inclusions Trigger Cellular Quiescence, Deactivate Apoptosis, and Lead to Delayed Necrosis. Cell Rep *19*, 919-927.

Rigort, A., Bauerlein, F.J., Villa, E., Eibauer, M., Laugks, T., Baumeister, W., and Plitzko, J.M. (2012a). Focused ion beam micromachining of eukaryotic cells for cryoelectron tomography. Proc Natl Acad Sci U S A *109*, 4449-4454.

Rigort, A., Gunther, D., Hegerl, R., Baum, D., Weber, B., Prohaska, S., Medalia, O., Baumeister, W., and Hege, H.C. (2012b). Automated segmentation of electron tomograms for a quantitative description of actin filament networks. J Struct Biol *177*, 135-144.

Ross, C.A., and Poirier, M.A. (2004). Protein aggregation and neurodegenerative disease. Nat Med *10 Suppl*, S10-17.

655   Roux, A. (2013). The physics of membrane tubes: soft templates for studying cellular
656   membranes. Soft Matter *9*, 6726-6736.
657   Saibil, H.R., Seybert, A., Habermann, A., Winkler, J., Eltsov, M., Perkovic, M., Castano-Diez,
658   D., Scheffer, M.P., Haselmann, U., Chlanda, P.*, et al.* (2012). Heritable yeast prions have a
659   highly organized three-dimensional architecture with interfiber structures. Proc Natl Acad Sci U
660   S A *109*, 14906-14911.
661   Scherzinger, E., Lurz, R., Turmaine, M., Mangiarini, L., Hollenbach, B., Hasenbank, R., Bates,
662   G.P., Davies, S.W., Lehrach, H., and Wanker, E.E. (1997). Huntingtin-encoded polyglutamine
663   expansions form amyloid-like protein aggregates in vitro and in vivo. Cell *90*, 549-558.
664   Schindelin, J., Arganda-Carreras, I., Frise, E., Kaynig, V., Longair, M., Pietzsch, T., Preibisch,
665   S., Rueden, C., Saalfeld, S., Schmid, B.*, et al.* (2012). Fiji: an open-source platform for
666   biological-image analysis. Nat Methods *9*, 676-682.
667   Tang, T.S., Tu, H., Chan, E.Y., Maximov, A., Wang, Z., Wellington, C.L., Hayden, M.R., and
668   Bezprozvanny, I. (2003). Huntingtin and huntingtin-associated protein 1 influence neuronal
669   calcium signaling mediated by inositol-(1,4,5) triphosphate receptor type 1. Neuron *39*, 227-239.
670   Trevino, R.S., Lauckner, J.E., Sourigues, Y., Pearce, M.M., Bousset, L., Melki, R., and Kopito,
671   R.R. (2012). Fibrillar structure and charge determine the interaction of polyglutamine protein
672   aggregates with the cell surface. J Biol Chem *287*, 29722-29728.
673   Vidal, R.L., Figueroa, A., Court, F.A., Thielen, P., Molina, C., Wirth, C., Caballero, B., Kiffin,
674   R., Segura-Aguilar, J., Cuervo, A.M.*, et al.* (2012). Targeting the UPR transcription factor XBP1
675   protects against Huntington's disease through the regulation of FoxO1 and autophagy. Hum Mol
676   Genet *21*, 2245-2262.
677   Waelter, S., Boeddrich, A., Lurz, R., Scherzinger, E., Lueder, G., Lehrach, H., and Wanker, E.E.
678   (2001). Accumulation of mutant huntingtin fragments in aggresome-like inclusion bodies as a
679   result of insufficient protein degradation. Mol Biol Cell *12*, 1393-1407.
680   Wegmann, S., Jung, Y.J., Chinnathambi, S., Mandelkow, E.M., Mandelkow, E., and Muller, D.J.
681   (2010). Human Tau isoforms assemble into ribbon-like fibrils that display polymorphic structure
682   and stability. J Biol Chem *285*, 27302-27313.
683   Woerner, A.C., Frottin, F., Hornburg, D., Feng, L.R., Meissner, F., Patra, M., Tatzelt, J., Mann,
684   M., Winklhofer, K.F., Hartl, F.U.*, et al.* (2016). Cytoplasmic protein aggregates interfere with
685   nucleocytoplasmic transport of protein and RNA. Science *351*, 173-176.
686   Yamamoto, A., Lucas, J.J., and Hen, R. (2000). Reversal of neuropathology and motor
687   dysfunction in a conditional model of Huntington's disease. Cell *101*, 57-66.
688   Zhang, H., and Hu, J. (2016). Shaping the Endoplasmic Reticulum into a Social Network. Trends
689   Cell Biol *26*, 934-943.
690